Supporting information for:

Transport into Nanosheets: Diffusion Equations Put to Test

Nils E. R. Zimmermann,* Timm J. Zabel, and Frerich J. Keil

Institute for Chemical Reaction Engineering, Hamburg University of Technology, Eissendorfer Str. 38, 21073 Hamburg, Germany

E-mail: nils.zimmermann@tu-harburg.de

*To whom correspondence should be addressed

Contents

1 Transient Molecular Dynamics

In the following section, we will highlight details on the transient molecular dynamics (TrMD) simulations performed in this work (Section 1.1), list the models used and approximations made (1.2), as well as present tests of TrMD specific parameters (1.3).

1.1 Simulation Details

As described in the main text, transient molecular dynamics (TrMD) is basically a mixture of equilibrium molecular dynamics (EMD) with spatially restricted Grand-Canonical Monte Carlo (GCMC) trials, the latter enabling a non-constant number of molecules in contrast to ordinary EMD.

Simulations were carried out in a rectangular simulation box, as depicted in Figure S1. Nanosheets were created by placing $N_{\mathrm{uc},x} \times N_{\mathrm{uc},y} \times N_{\mathrm{uc},z}$ unit cells in the box center (AFI: 2×2 in x and y as well as 3, 6, 12, 24, and 48 along z coordinate for enabling increasing nanosheet thickness; LTA: 3×3 in x and y as well as 6, 12, and 24 in z). In addition, we added a layer of half a unit cell along z in case of AFI. In contrast to x and y, void space was added along z in order for a gas space to establish. Since periodic boundary conditions were used in all directions, the set-up resembled an infinitely repeating sequence of nanosheets and gas space along z which extended infinitely in x and y. Both surfaces, AFI and LTA, concluded with the respective window rings so that the entropic diffusion bottle-necks formed the entrances to the pore structures in both cases.

At the left and right end of the simulation box, the control volumes, each of 16 Å width in z direction, were placed inside the gas space. Since the total void space added to the centered zeolite sheet amounted to 56.01 Å an 12.005 Å thick intermediate “buffer zone” was formed between the end of the CV and the position of the first zeolite atoms in z direction (Figure S1). Therefore, molecules located in the control volumes did not interact with the zeolite atoms because our potential cutoff radius was smaller than this buffer length (cf., Section 1.2). This, in turn, assured an unbiased gas behavior in the control volume. Note that the control volumes on each end of the

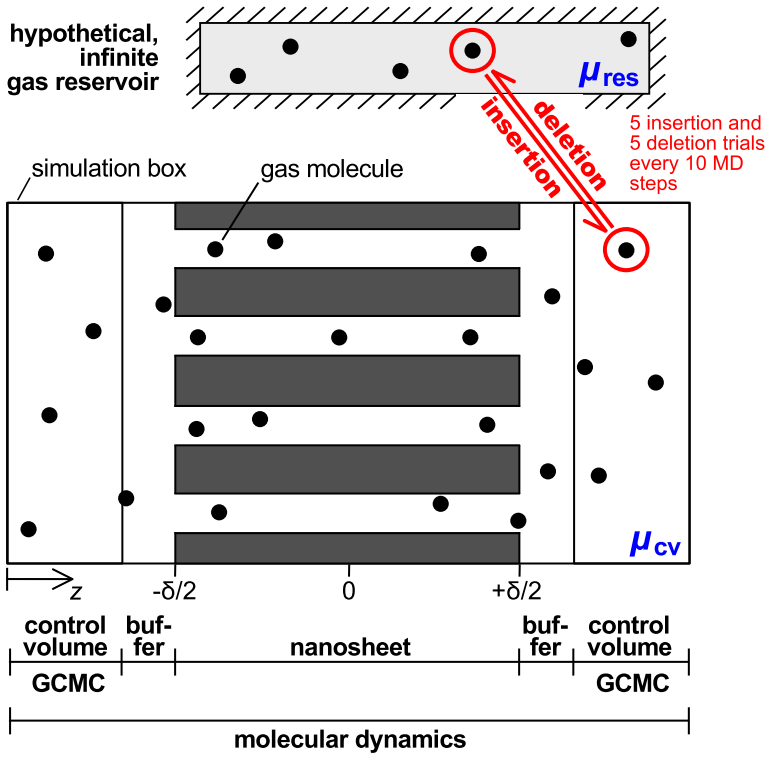

Figure S1: Scheme illustrating the simulation set-up and procedure.

simulation box formed in fact a single control volume due to the application of periodic boundary conditions in all directions. Hence, the size of the single control volume was 2×16 Å=32 Å.

The simulation set-up mimics situations encountered in diffusion measurements, such as uptake experiments, as well as interference[1] and infrared microscopy,[1] where the zeolite crystal is initially empty and then starts to be filled with gas molecules as time proceeds. In the experiments, the huge surrounding that is several magnitudes larger than the pore volume of the small crystal sample forms practically an infinite reservoir of gas molecules that can enter the pores of the solid. In our simulations, the control volume, which is of similar size as the pore volume, takes over the task of steady molecule supply because it is coupled to a hypothetical infinite gas reservoir via the GCMC trials.

We imposed a constant chemical potential, μ_{cv}, in the control volume by standard Grand-Canonical insertion and deletion trials. Every ten MD steps, five molecule insertion as well as five molecule deletion trials were performed inside the control volume. The acceptance probability of

an insertion trial to the control volume, $\mathrm{acc}(N_{\mathrm{cv}} \rightarrow N_{\mathrm{cv}}+1)$, reads[2,3]

$$\mathrm{acc}(N_{\mathrm{cv}} \rightarrow N_{\mathrm{cv}}+1) = \min\left[1, \frac{V_{\mathrm{cv}}}{\Lambda^3(N_{\mathrm{cv}}+1)} \exp\left\{\beta\left[\mu_{\mathrm{cv}} - U(N_{\mathrm{cv}}+1) + U(N_{\mathrm{cv}})\right]\right\}\right] \qquad (1)$$

where N_{cv} denotes the number of molecules in the control volume, V_{cv} its size, Λ the thermal de Broglie wavelength which equals $\sqrt{h^2/(2\pi m k_{\mathrm{B}} T)}$, h is Planck constant, m the mass of the just inserted particle, k_{B} Boltzmann constant, T the temperature imposed, $U(N_{\mathrm{cv}})$ and $U(N_{\mathrm{cv}}+1)$ the total potential energy of the old (N_{cv}) and new ($N_{\mathrm{cv}}+1$) state, respectively, as well as $\beta = 1/(k_{\mathrm{B}}T)$. However, it is more practical to impose the fluid-phase pressure because p can be converted into the fugacity, f, by an equation of state (here: Peng-Robinson) which can be incorporated directly into the acceptance probabilities.[2] Therefore, the insertion acceptance probability in fact used in our simulation code is

$$\mathrm{acc}(N_{\mathrm{cv}} \rightarrow N_{\mathrm{cv}}+1) = \min\left[1, \frac{V_{\mathrm{cv}}\beta f}{(N_{\mathrm{cv}}+1)} \exp\left\{-\beta\left[U(N_{\mathrm{cv}}+1) - U(N_{\mathrm{cv}})\right]\right\}\right]. \qquad (2)$$

The derivation of this equation is found in Appendix G of Frenkel's and Smit's seminal molecular simulation book.[2] The corresponding acceptance probabilities of a deletion trial, $\mathrm{acc}(N_{\mathrm{cv}} \rightarrow N_{\mathrm{cv}}-1)$, are[2]

$$\mathrm{acc}(N_{\mathrm{cv}} \rightarrow N_{\mathrm{cv}}-1) = \min\left[1, \frac{\Lambda^3 N_{\mathrm{cv}}}{V_{\mathrm{cv}}} \exp\left\{-\beta\left[\mu_{\mathrm{cv}} + U(N_{\mathrm{cv}}-1) - U(N_{\mathrm{cv}})\right]\right\}\right] \qquad (3)$$

$$\mathrm{acc}(N_{\mathrm{cv}} \rightarrow N_{\mathrm{cv}}-1) = \min\left[1, \frac{N_{\mathrm{cv}}}{V_{\mathrm{cv}}\beta f} \exp\left\{-\beta\left[U(N_{\mathrm{cv}}-1) - U(N_{\mathrm{cv}})\right]\right\}\right] \qquad (4)$$

with $(N_{\mathrm{cv}}-1)$ representing the new state (molecule deletion).

We performed 100,000 GCMC trials prior to the transient MD simulation itself to equilibrate the CV where the probability to perform an insertion trial was equal to the one of a deletion trial (50 %). A single trial position for the first bead was used to grow a new molecule in the control volume. Cell lists were used for speeding-up the computation of potential energies. Freshly inser-

ted molecules were assigned velocities that corresponded to the Maxwell-Boltzmann distribution of the molecule and the temperature imposed.

The velocity Verlet algorithm was used to numerically propagate the systems during the MD phase with a time-step size of 1 fs. As for the MD part of the transient MD simulations, we used neighbor lists to speed up the calculation of forces with a cutoff radius of 16 Å and a update frequency of 10 steps, that is, after each Monte Carlo phase. A Nosé-Hoover chain thermostat maintained the temperature imposed.[4] Although the length of the simulations were always set to 2 μs, we have usually stopped them as soon as the uptake curve showed a well appreciable plateau at unity. In two cases, however, the simulations did not attain this value because of an unexpected shutdown of our computer cluster: AFI simulations with the thickest sheet [$m(t)/m_{\text{final}} = 0.85$] and LTA calculations using the intermediate sheet thickness [$m(t)/m_{\text{final}} = 0.93$].

Room temperature (300 K) was imposed in the AFI simulations, whereas T was set to 750 K in case of LTA. Preliminary tests using conventional equilibrium molecular dynamics (EMD) at room temperature have clearly shown that methane diffusivities are exceptionally small in LTA ($\approx 2 \times 10^{-11}$ m^2/s). The low temperature would have prohibited long enough transient MD simulations of methane at room temperature with increasing nanosheet thickness. In fact, the simulations at 750 K employing the thickest LTA sheet were already such time-consuming that a single run took, on an average, 88 days on a state-of-the-art Intel quad-core cluster![*] Noting that the diffusivities at 750 K amounted to roughly 6×10^{-10} m^2/s leads to an increase in the diffusion coefficient by a factor of 30. Taking the opposite point of view, a single TrMD simulation would in first order approximation have taken 30×88 days $= 2640$ days at room temperature, obviously being infeasible. Furthermore, we have to reiterate that 40 independent simulation runs were performed in order for the concentration profiles and uptake curves to show little noise and thus providing statistically significant data (cf., Figure 2a and b in the main text). This sums up to remarkable 40×88 days $= 3520$ days ≈ 10 years of single-core cluster time that were necessary for the most

[*]The cluster was purchased from COMPTRONIC GmbH, Germany, and is based on SuperMicro-Barebone systems. Each node has two quad-core CPUs (Intel XEON Harpertown E5430 and XEON Nehalem X5550) where each core has a performance of 2.66 GHz. The RAM ranges between 16 and 24 gigabyte per node and thus 2 to 3 gigabyte per core. Operating system is SuSE SLES 11.

demanding system in fact studied in this work (thickest LTA sheet).

The pressure imposed on the control volume was 10 bar and 100 bar for AFI and LTA, respectively. The saturation concentration at the end of the TrMD simulations agreed perfectly with the adsorption isotherms obtained from conventional Grand-Canonical Monte Carlo simulations and amounted to $c_{\text{final}} = 1872$ mol/m^3 and 994 mol/m^3 for AFI and LTA, respectively. The corresponding loadings were 0.78 and 1 molecule per cage, indicating that the higher pressure in LTA simulations compared to AFI runs was necessary to ensure comparable adsorption conditions.

Concentration profiles were obtained by dividing the nanosheet into equally sized slabs with respect to the *z* coordinate. The slab width was set to the cage size, l_{cage}, of the respective structure. The slab borders were set to the window locations where molecules "feel" the diffusion bottleneck (Figure S2). We have to stress here that the slab containing the outermost cage on either side of the sheet was ignored, as indicated by the X's in Figure S2. By this, we circumvented the influence of lower adsorption in the nanosheet boundary region on the transport coefficients. We have recently shown[5] that this effect makes the tracer-exchange diffusion coefficient, D_{S}, and surface permeability, α_{S}, decrease with increasing sheet thickness δ. Therefore, we conclude that the decrease of both α and D_{T} as observed in the present work for AFI is very likely caused by the memory effect only.

An order-*n* scheme[2] was adopted for sampling of transient concentration profiles, $c(t,z)$. This has been proven to be very helpful because the short time uptake behavior is decisive for accurate determination of the surface permeability, which we had already learned during the analysis of our previous work on tracer-exchange surface permeabilities.[5] In this respect, we observed that the thinner the membrane or sheet is, the more important will be data at early uptake stages. In conventional schemes where constant sampling frequencies are used to save concentration profiles (i.e., linear in time), short time intervals would have been necessary for a reliable determination of α. This, however, would have led to an extremely high number of total sampling points. Obviously not being efficient from a memory point of view, the linear sampling is neither wanted in regard of the CPU time that would be necessary to fit the resulting exceptionally large number of profiles

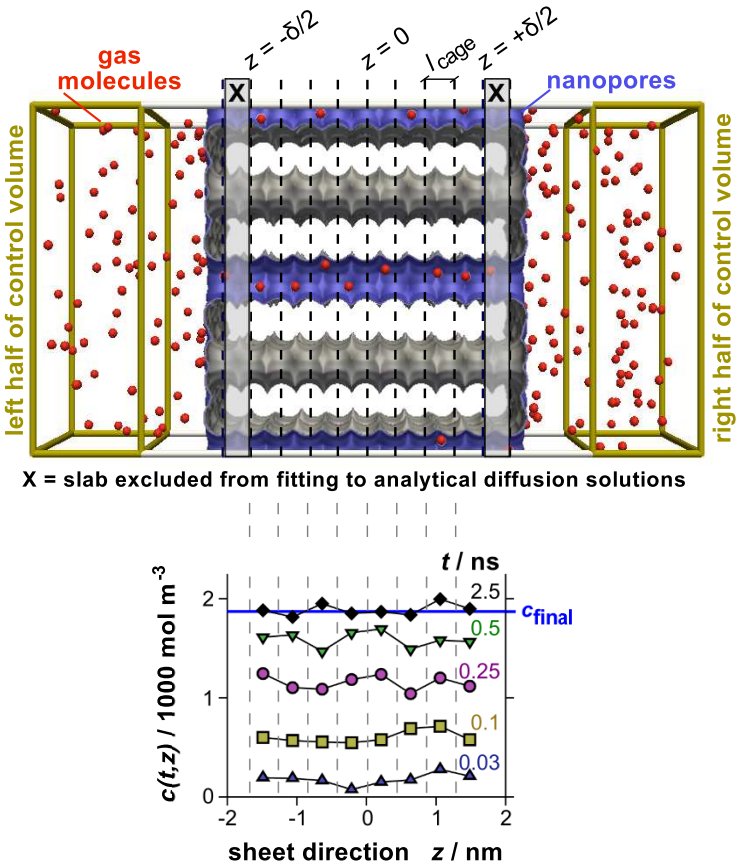

Figure S2: Scheme illustrating the sampling of the concentration profiles. Note that we do not show concentration profiles from a single TrMD simulation but profiles averaged over 40 independent TrMD simulations for reasons of clarity.

with different diffusion models having various parameters. Therefore, we sampled concentration profiles every 100$^{\text{th}}$ step for the first 1000 MD steps and, after these initial 1000 steps (=1 ps), switched over to an order-*n* scheme. Each order of magnitude was divided into 20 blocks, thus yielding 20 *c*-profiles per time magnitude.

At each *c*-profile sampling time, we recorded the numbers of molecules that were found in the individual slabs, divided these numbers by $N_{\text{A}} \times V_{\text{slab}} = N_{\text{A}} \times l_{\text{box},x} \times l_{\text{box},y} \times l_{\text{cage}}$, and saved the resulting profile. We observed that profiles from single TrMD simulations were very noisy. Therefore, 40 separate, independently initialized TrMD simulations were performed per system in order to average the noisy single-simulation concentration profiles. In this respect, we have to add that the time origin was shifted to the last concentration-profile sampling instance at which all

concentrations of the averaged profile (i.e., along z) were zero.

Uptake curves, $m(t)/m_{\text{final}}$, were calculated by integrating the concentration profiles, $c(t,z)$, with respect to the sheet width z and normalizing the values with the integral of the saturation concentration thus yielding

$$\frac{m(t)}{m_{\text{final}}} = \frac{\int_{-\delta/2}^{+\delta/2} c(t,z)\,\mathrm{d}z}{\int_{-\delta/2}^{+\delta/2} c_{\text{final}}\,\mathrm{d}z}. \tag{5}$$

The integration limits highlight that the origin was located in the center of the nanosheet, whose thickness was δ.

1.2 Models

Methane was modeled as a single united atom bead that interacts via a Lennard-Jones type potential with any other methane bead[6]

$$U_{i,i}(r) = 4 \cdot \varepsilon_{i,i} \cdot \left[\left(\frac{\sigma_{i,i}}{r} \right)^{12} - \left(\frac{\sigma_{i,i}}{r} \right)^{6} \right] \tag{6}$$

where $U_{i,i}(r)$ represents the potential energy, U, between two Lennard-Jones united atoms of same kind, i,i, that are a distance r apart from one another in space, and $\varepsilon_{i,i}$ as well as $\sigma_{i,i}$ denote the respective Lennard-Jones parameters (well-depth and zero-potential distance of the interaction between two beads of same type i). The interaction with the siliceous zeolite structure consisted also of a Lennard-Jones potential only,[6] such that the subscripts in Eq. (6) change from i,i (same bead kinds) to i,j for signifying different parameters because of the potential being calculated for unlike beads.

The inclusion of partial charges has not been advisable because of two reasons. First, it is well-known that the interaction of saturated hydrocarbons are almost exclusively governed by dispersive van-der-Waals interactions, given that no chemical reaction is to be expected. This fact justifies a purely Lennard-Jonsian potential between guests and guests as well as guests and siliceous zeolite

host structure. Second, any electrostatic term would have disproportionately increased the computational burden where we have to stress again that many (40) independent, long running simulations were necessary to obtain smooth concentration profiles at all relevant stages of nanosheet filling. Therefore, a good tradeoff between realistic description of the system under study and minimization of computational costs was an important aspect of this work. For example, we decided furthermore not to employ potential grids in the zeolite interior to speed-up guest-host interaction calculation.[7] Such lookup tables might have introduced transport artefacts due to slight potential singularities at the border between the region of fully explicit interaction calculation and grid region. Instead, we used cell lists during the GCMC phase, as highlighted in Section 1.1, which accelerated simulation runs by a factor of 2.2. Grids, on the contrary, can lead to an enhancement of simulation performance by as much as a factor of 12.6. We have to point out that these comparative performance data are based on adsorption isotherm calculations in a periodic AFI zeolite with GCMC at 300 K and 10 bar in which the simulation box was approximately as large as the thickest AFI nanosheet studied here. The (relative) computational burden was therefore comparable to the most demanding nanosheet simulations because the number of zeolite atoms, which mainly determines the number of interactions to be calculated, was roughly the same (periodic vs nanosheet) and the number of adsorbate molecules maximal (nanosheet saturation at pressure of interest).

In the light of a good tradeoff between realistic modeling and computational efficiency, it is also important to note that we have dealt with rather simple and idealized surfaces that were not chemically saturated by silanol groups[3] or the like. While such groups can lead to a five-fold decrease in the surface permeability,[3] the computational burden would rise dramatically. This is, because corresponding force fields would again require the inclusion of partial charges. We decided to use the computationally more efficient, though less realistic surface to enable a thorough study of the effect induced by the nanosheet thickness, being the primary focus of this work.

The potential energies and the forces were only explicitly calculated up to a cutoff distance of $r_{\text{cutoff}} = 12$ Å. To avoid any singularities in both the potential energy (MD and MC) and the

forces (MD only), the cut potential was shifted to zero at the cutoff, which is in accordance with the original force field[8] and yields (for same beads; cf. Eq. (6)):

$$U_{i,i}(r) = \begin{cases} 4 \cdot \varepsilon_{i,i} \cdot \left[\left(\frac{\sigma_{i,i}}{r} \right)^{12} - \left(\frac{\sigma_{i,i}}{r} \right)^{6} \right] & \text{if } r < r_{\text{cutoff}} \\ 0 & \text{otherwise} \end{cases} \tag{7}$$

The role of zeolite-lattice flexibility has been a controversial topic since the very beginnings of simulation studies on guest-molecule adsorption[9] and transport[10,11] in these nanoporous host materials. But most evidence points today at the fact that the influence is minor, particularly for rather small molecules such as methane.[12–15] Purely dynamic effects, such as the "breathing window",[10] do most likely not have any significant influence. The term refers to the idea that the window atoms of a zeolite structure move as soon as a guest molecule appears so that the window size increases and the passage of the guest molecule is considerably facilitated. However, "static" effects, such as the average window size, have been proven to be very crucial to transport in zeolites.[12–15] In this light, the modeling approach chosen again proves to be realistic enough for drawing valid "real-world" conclusions while being efficient for the demanding transient molecular dynamics simulations.

Consistent with the original force field,[6,8] the interaction between methane molecules and the zeolite structures was assumed to be dominated by the CH_4-O part, in fact entirely neglecting any contribution by silicon atoms. While this can also be seen as a tradeoff between realistic description and computational feasibility, the approximation is physically senseful because the zeolite structures can be regarded to consist of O^{2-} and Si^{4+} ions where the large oxygen ions shield the smaller silicon ions.

1.3 Parameter Tests

Since the control volume and thus its size as well as the number of GCMC trials performed are rather specific parameters to TrMD simulations we have tested their influence on the basis of

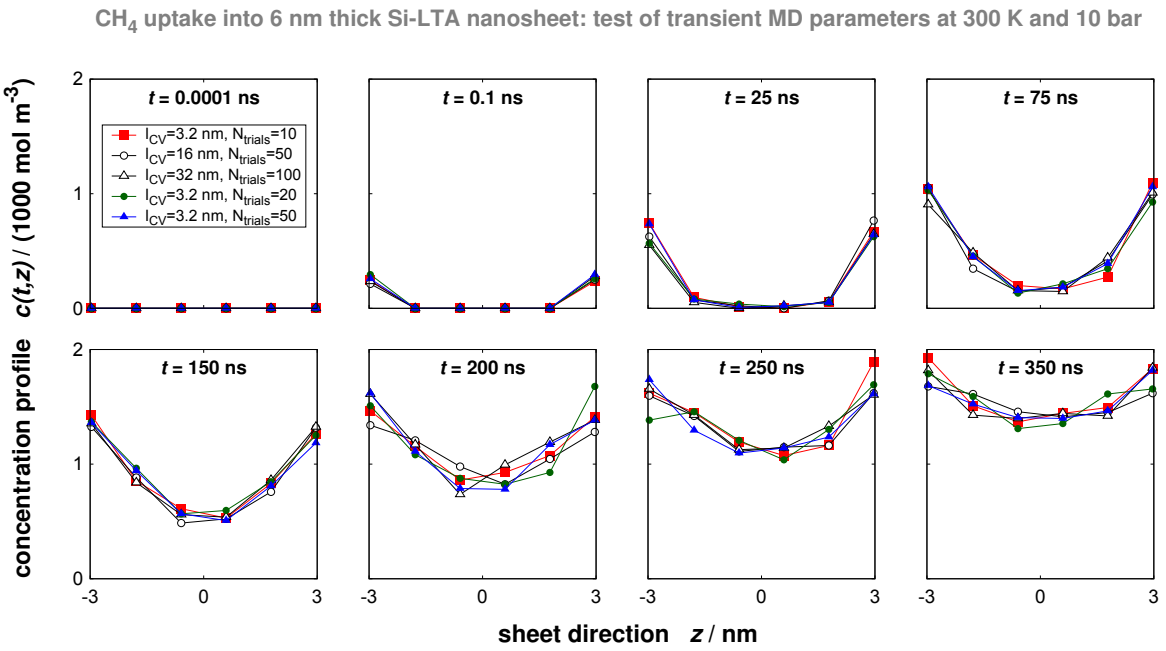

Figure S3: Concentration profiles of methane uptake into the smallest LTA nanosheet studied ($\delta \approx 6$ nm) at 300 K and 10 bar and for different widths of the control volume, l_{cv}, as well as different numbers of GCMC trials (N_{trials} = insertion plus deletion) during each GCMC phase. Each profile represents an average from 15 independent simulations under same conditions.

methane uptake into the smallest LTA nanosheet at 300 K and 10 bar. The frequency of switching from MD to GCMC is also an important and specific quantity. But it has been shown elsewhere for similar systems[16,17] that every tenth MD step should be high enough a frequency to ensure steady supply to the control volume and, hence, to simulate a stable gas reservoir. In the references given, the highest frequency was every 20^{th} MD step.

Keeping all other parameters constant, the size of the control volume (total width) was varied from $l_{\mathrm{cv}} = 2 \times 1.6$ nm $= 3.2$ nm over 2×8 nm $= 16$ nm to 2×16 nm $= 32$ nm. To ensure the same GCMC trial rate per volume, the number of GCMC trials (N_{trials} = insertion plus deletion) was proportionately adjusted to the control volume length; thus, $N_{\mathrm{trials}} = 10$, 50, and 100. However, the influence of the number of GCMC trials was also investigated by varying it from 10 over 20 to 50 for a constant control volume size of 3.2 nm. Note that we performed as many insertion ($N_{\mathrm{trials}}/2$) as deletion attempts ($N_{\mathrm{trials}}/2$) per GCMC phase.

A sequence of resulting concentration profiles is shown in Figure S3 for the parameter combi-

nations studied. At any time, the profiles fall on top of one another, subject to only minor deviations in consequence of statistical fluctuations. Clearly, the parameters have no influence on the filling of the nanosheet with methane molecules in the ranges investigated. Therefore, we used the most efficient setup, that is, the smallest control volume width (3.2 nm) and the smallest number of GCMC trials (10).

2 Methodology Verification

In this section, we will verify the methodology outlined in Section 1 by comparing data from measurements on adsorption and transport properties with results of conventional equilibrium Grand-Canonical Monte Carlo (GCMC) and standard equilibrium molecular dynamics (EMD) simulations (Section 2.1). Furthermore, we deduce transport-diffusion coefficients from EMD and GCMC in Section 2.2 which are compared to transport-diffusion coefficients obtained from TrMD (main text).

Following differences applied to the GCMC simulations in comparison with simulation details and parameters used in TrMD simulations. Potential grids with finenesses of 0.038 and 0.065 Å for AFI and LTA, respectively, were used to speed-up the calculations between adsorbate molecules and zeolite atoms. While the MC library of insertion and deletion trials was extended to also include translational displacements of the methane molecules, rotational trials were not of concern because methane was modeled as a single spherical Lennard-Jones bead. We imposed a target acceptance probability for the displacement trials of 50 %. Therefore, the maximum displacement distance, in compliance with common practice, was dynamically adjusted during the simulation to match this probability on an average,[2] starting with a value of 1 Å in the equilibration phase of each GCMC simulation. Furthermore, we have typically performed 80 displacement trials and 40 transfer (= insertion plus deletion) trials per MC cycle where 25,000 equilibration and 12,500,000 production MC cycles were executed per pressure point of a given isotherm. The maximum displacement distance was adjusted every 125,000$^{\text{th}}$ cycle, thus yielding 100 displacement adjustments in the isotherm production phase per state point. At higher pressures, we had to reduce the number of production cycles to 5,000,000, which, however, did not compromise the statistics of the adsorption isotherm to any appreciable extent. For example, the relative error of methane adsorption in AFI at 300 K and 10 bar (final state point of our TrMD simulations) was 0.06 % executing 12,500,000 cycles, whereas still as small an error as 0.09 % was achieved at 20 bar performing only 5,000,000 cycles. Finally, the GCMC simulation boxes consisted of $2\times2\times25$ and $3\times3\times6$ unit cells in case of AFI and LTA, respectively.

In case of EMD simulations (*NVT* ensemble), following differences apply in comparison to the TrMD runs. Just as for GCMC, potential grids were used in the periodic EMD simulations but here with finenesses of 0.061 and 0.052 Å for AFI and LTA, respectively. Usually, each EMD simulation was conducted until the system reached 500 to 1000 ns. Long simulation boxes were used at low concentrations in AFI (2×2×25 unit cells) to cope with a known channel-length effect that we have investigated previously.[12] However, to reduce the computational burden with increasing concentration, the boxes were proportionately reduced in size which was legitimate because the channel-length effect levels off as concentration increases.[12] For LTA, this effect is absent but we have encountered that the thermostat has some biasing influence on the diffusion coefficient which we discuss in Section 2.2.

EMD simulations provided both mean squared displacement (MSD) of single-molecule motion along z direction, $1/N \cdot \sum_{i=1}^{N} [z_i(t) - z_i(0)]^2$, as well as squared mean displacement (SMD) of the center-of-mass motion of all guest molecules along z, $\{1/N \cdot \sum_{i=1}^{N} [z_i(t) - z_i(0)]\}^2$. The self-diffusion coefficient for the z direction, $D_{\mathrm{S},z}$, was obtained via the slope of the MSD

$$D_{\mathrm{S},z} = \frac{1}{2} \lim_{t\to\infty} \frac{\mathrm{d}}{\mathrm{d}t} \left\langle \frac{1}{N} \sum_{i=1}^{N} \left[z_i(t) - z_i(0) \right]^2 \right\rangle, \tag{8}$$

In Eq. (8), N denotes the number of molecules of the species for which the diffusive motion is to be calculated and $z_i(t)$ the position of molecule i along z coordinate at time t, whereas the angular bracket indicate an ensemble average, that is, the MSD has to be computed for many different reference points $z_i(0)$. The corrected diffusion coefficient, $D_{\mathrm{C},z}$, which is sometimes also referred to as the collective diffusion coefficient because it rates the mobility of the entire center-of-mass of all molecules at once, was calculated by the SMD slope

$$D_{\mathrm{C},z} = \frac{1}{2} \lim_{t\to\infty} \frac{\mathrm{d}}{\mathrm{d}t} \left\langle \left\{ \frac{1}{N} \sum_{i=1}^{N} \left[z_i(t) - z_i(0) \right] \right\}^2 \right\rangle. \tag{9}$$

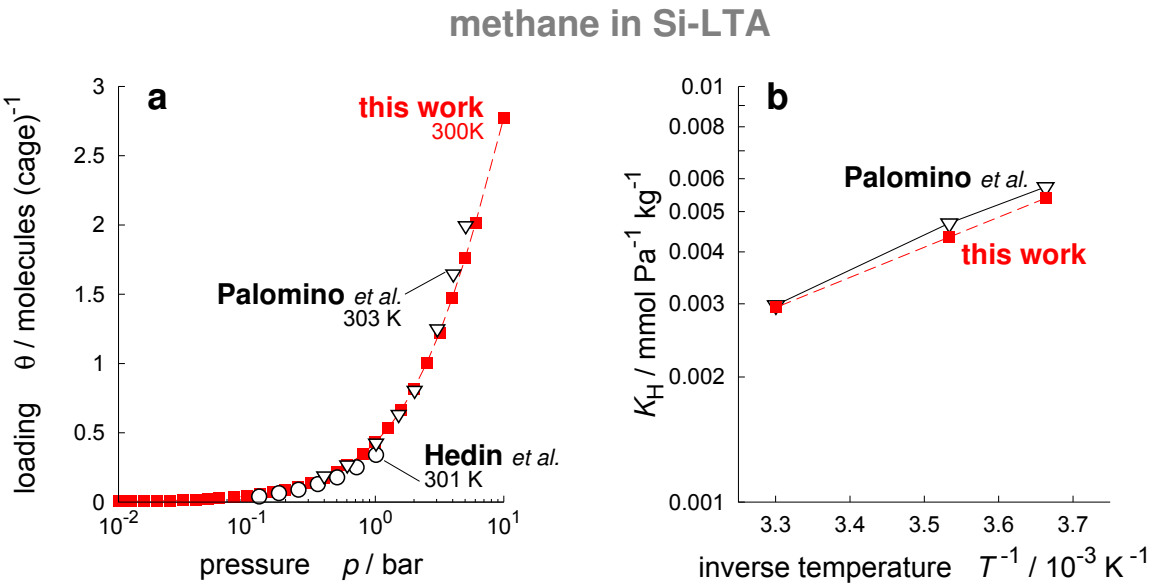

Figure S4: Adsorption isotherm at 300–303 K (a) and Henry coefficients over inverse temperature (b) for methane in purely siliceous LTA-type zeolites from volumetric and gravimetric measurements (Hedin et al.:[20] open circles; Palomino et al.:[21] open triangles) as well as from molecular Monte-Carlo simulations (this work: red filled squares). Note that statistical uncertainties of the simulation results are smaller than the symbol size.

2.1 Agreement between Simulations and Measurements

Dubbeldam's force field[8] was employed because it was specifically and carefully developed to reproduce experimental adsorption isotherms by fitting to inflection points[6,8] and showed good agreement with diffusion measurements, too.[18] In the following, we reassess the quality of the model.

In Figure S4, we present experimental adsorption data for methane in siliceous LTA[19] (Ref. 20 and 21) and our molecular simulation predictions. Deviations amount to at most 12 % (Ref. 21) and 30 % (Ref. 20) between isotherms obtained from measurements and from Grand Canonical Monte Carlo (Figure S4a). This is a good result considering the fact that rather small perturbations in the crystal structure can easily lead to exactly this magnitude of loading discrepancy.[22] The deviations in the Henry coefficients (Figure S4b) range between −1 % and −8 %, both indicating the exceptional good agreement at low loadings.

Hedin et al.[20]m also determined the self-diffusion coefficient of methane in Si-LTA at 301 K and 1.013 bar ($\hat{=}$ 0.4 molecules per cage) by means of PFG-NMR measurements:

- $D_S = 1.42\times10^{-10}$ m^2/s.

Note that the diffusivity is averaged over all three Cartesian components:

$$D_S = \frac{D_{S,x} + D_{S,y} + D_{S,z}}{3}, \tag{10}$$

where it is noteworthy that LTA is an isotropic medium to methane diffusion such that $D_S = D_{S,x} = D_{S,y} = D_{S,z}$. Our molecular dynamics prediction amounts to

- 0.293×10^{-10} m^2/s

using Dubbeldam's force field at 300 K and 0.4 molecules per cage. The comparison reveals as large a deviation between experiment and simulation as a factor of 4.8. This is however not surprising because deviations in transport coefficients (experiments vs simulations) often span several orders of magnitude,[23] particularly if the diffusivities are small. Moreover, PFG NMR experiments for small hydrocarbons in Si-LTA notoriously yield inconsistent results. Orders-of-magnitude discrepancies in diffusion coefficients are observed just by using crystallites from different synthesis batches.[24] Therefore, we regard a factor of roughly five between our prediction and Hedin's measurement as a positive outcome.

Although we have not found any experimental adsorption and transport data of methane in SSZ-24, the siliceous AFI-type zeolite structure,[25] there are data for a similar structure with the same framework type: $AlPO_4$-5,[26] the aluminum phosphate equivalent to SSZ-24. The experimental data[27–31] are displayed in Figure S5 along with our simulation predictions. We observe over-predictions in adsorption (Figure S5a) up to a factor of 2.4 at 97 K and low pressures (4×10^{-6} bar). However, this levels off quickly to small differences between 7 % to 18 % from 2×10^{-5} bar on. Importantly, inflection points are well reproduced. They usually give rise to reordering processes of the adsorbate molecules in the host structure and, hence, serve as an additional indicator of

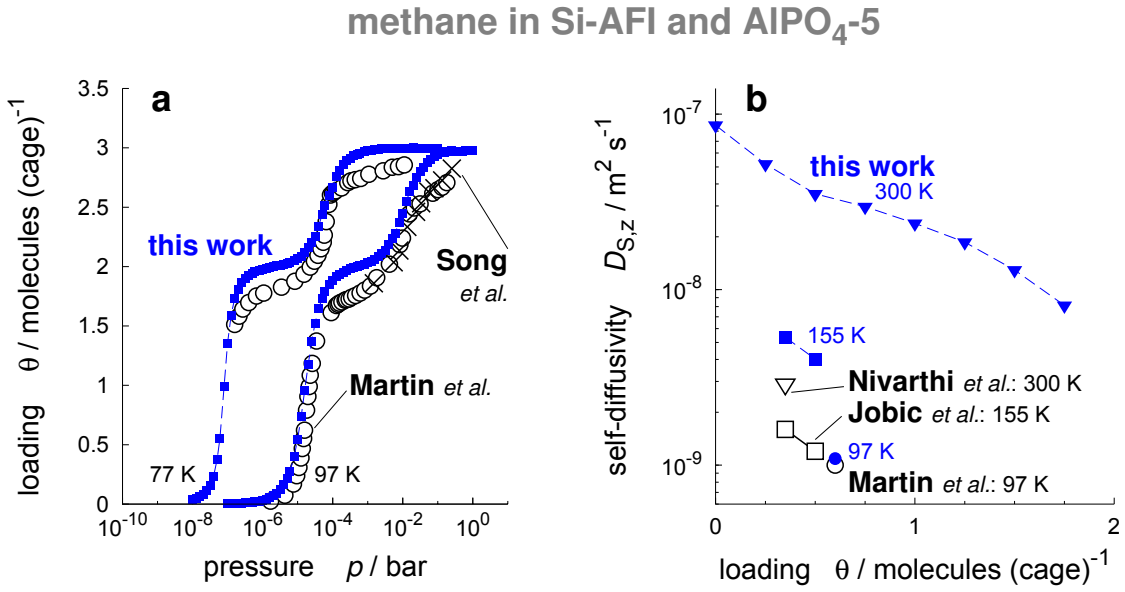

Figure S5: Adsorption isotherms at 77 K and 97 K (a) as well as self-diffusion coefficients over loading at various temperatures (b) for methane from measurements in $AlPO_4$-5 (Martin et al.:[27,28] open circles; Song et al.:[29] crosses; Nivarthi et al.:[30] open triangle; Jobic et al.:[31] open squares) and from molecular simulations in silicious AFI (this work: blue filled symbols), respectively.

realistic modeling apart from the mere quantitative agreement.[32] Taken together, we conclude that adsorption isotherms are reasonably reproduced.

The comparison of methane self-diffusion coefficients in AFI (Figure S5b) shows that we obtain good agreement with the experiments at the lowest temperature (97 K) only. As the temperature is raised, the discrepancy between measurement (open symbols) and prediction (filled symbols) increases to more than an order of magnitude. Note here that the statistical accuracy of the simulation is very high because the error bars, plotted along with our simulation data, are much smaller than the symbol sizes. The experimental error, on the other hand, is rather large with an estimated value of 50 % as given in Ref. 31 for the diffusivities at 155 K. Such large uncertainties do however not explain a more than 10-fold deviation at 300 K. We can only speculate about the reasons why the discrepancy increases with temperature. The most likely explanation, in our opinion, are differences in $AlPO_4$-5 crystallites, as was also suggested by Jobic et al.[31] For example, different $AlPO_4$-5 batches could have had different degrees of lattice defects which formed

internal transport resistances[1] in addition to the intrinsic diffusion barriers caused by the perfect nanopore.[32] This is quite probable because some zeolitic materials,[33] just as $AlPO_4$-5,[34] are sensitive against storage under non-dry conditions. The different degree of (hypothetical) defects may have been pure coincidence, but it is also possible that there is a relationship between intrinsic diffusion barriers, transport resistances by lattice defects and temperature. While the hypothesis is scientifically appealing, its investigation is beyond the scope of this work. We therefore conclude that the force field chosen describes methane self-diffusion in AFI-type zeolites well enough for our purposes, given the facts that experimental and simulation results were based on slightly different host structures and that the experimental errors were rather large. However, we have to stress that a lower prediction certainty exists as compared to the above discussed transport in LTA because of larger discrepancies between measurements and simulations in case of AFI.

2.2 Transport-Diffusion Coefficient from EMD

To compare diffusion coefficients from transient MD simulations (main text) with diffusivities from equilibrium MD we use the thermodynamic correction factor, Γ.[35] The factor is defined for single component adsorption under isothermal conditions by the change in the logarithm of the fugacity, $\partial \ln f$, with change in logarithm of equilibrium concentration in the adsorbed zeolite phase, $\partial \ln c_{\mathrm{eq,zeol}}$:

$$\Gamma \equiv \left. \frac{\partial \ln f}{\partial \ln c_{\mathrm{eq,zeol}}} \right|_T . \tag{11}$$

The thermodynamic correction factor links the corrected diffusion coefficient, D_{C}, with the transport-diffusion coefficient, D_{T}, via[36]

$$D_{\mathrm{T}}(c_{\mathrm{eq,zeol}}) = \Gamma(c_{\mathrm{eq,zeol}}) \times D_{\mathrm{C}}(c_{\mathrm{eq,zeol}}), \tag{12}$$

where all three quantities usually depend on guest concentration, $c_{\mathrm{eq,zeol}}$, in the adsorbed zeolite phase. The equation originates from deriving the diffusion equations on the basis of an energy balance where the chemical potential driving force is opposed by a friction force.[36] From a scientific

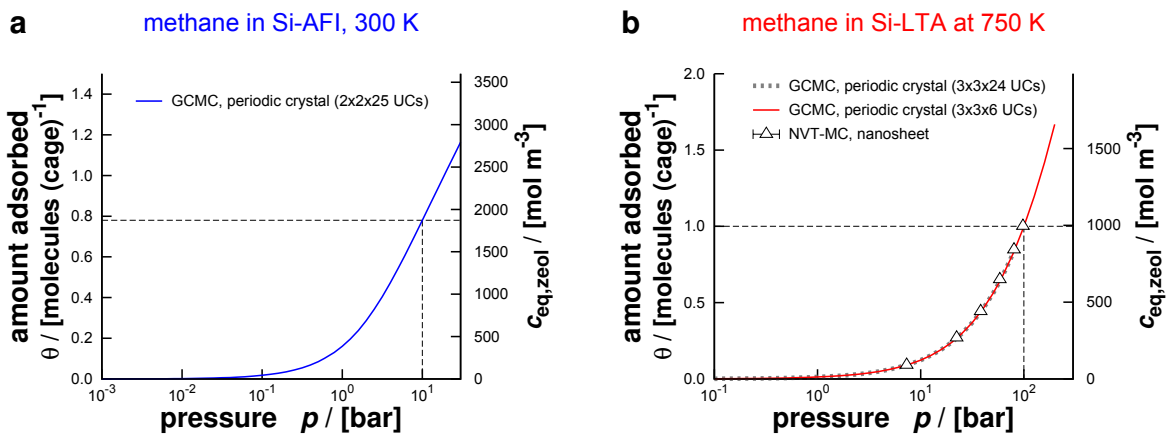

Figure S6: Adsorption isotherms of methane in siliceous AFI at 300 K (a) and in siliceous LTA at 750 K (b) obtained from GCMC simulations in periodic zeolite crystals (solid and dotted lines). Vertical and horizontal dashed lines highlight final equilibrium state points of the transient MD simulations. Triangles in part b are isotherm results from NVT-MC instead of GCMC where, however, the simulation box contained an explicit gas space. In that case, the gas-phase pressure was calculated on the basis of the average gas-phase concentration via the Peng-Robinson equation of state.

point of view, it provides an ideal means to investigate diffusion phenomena because the relative significance of thermodynamic effects (Γ) and mobility effects (D_C) on the transport diffusivity can be extracted.[36] It is at this point noteworthy that many authors in zeolite science prefer to present diffusion coefficients as functions of loading (θ), that is, in molecules per unit cell or cage, but that both quantities are directly related ($\theta \propto c_{eq,zeol}$).

The comparison of diffusion coefficients requires thus the calculation of corrected diffusion coefficients as well as adsorption isotherms, the latter being used for the numerical determination of Γ. Therefore, we show the adsorption isotherms of methane in AFI at 300 K and in LTA at 750 K obtained from GCMC simulations in Figure S6. The final equilibrium states of the transient MD simulations are indicated by dashed lines. Evidently, the two states are at comparable isotherm locations. Note that we have tested whether or not the LTA isotherm is sensitive against changes in simulation box size. We could successfully rule out such biasing influence, as evidenced by the comparison between solid line in Figure S6b (small simulation box) and dotted line (large box).

Results of corrected diffusion coefficients from EMD simulations are presented in Figure S7.

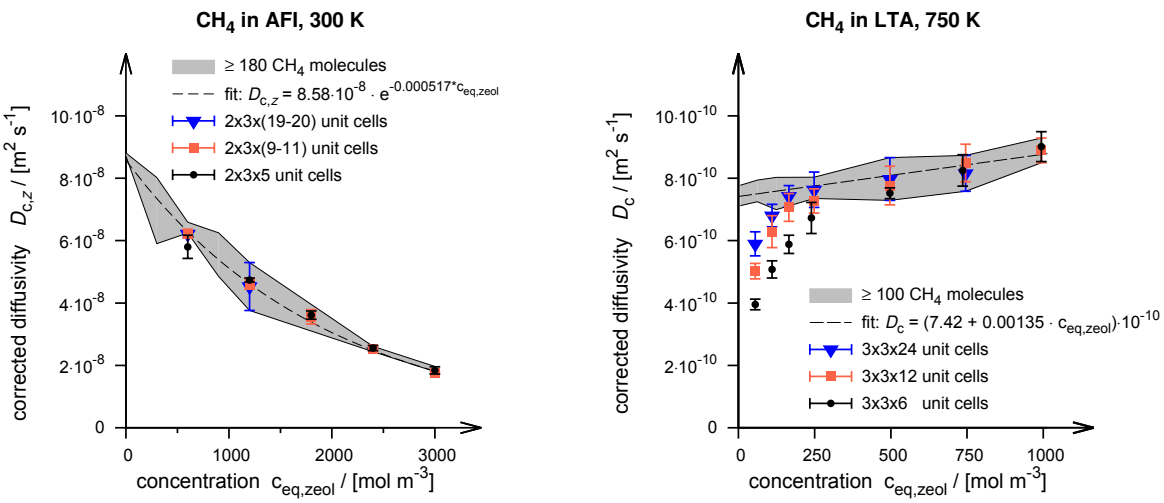

Figure S7: Corrected diffusion coefficients of methane in AFI at 300 K (left) and LTA at 750 K (right) from equilibrium molecular dynamics simulations (NVT). Note again that LTA is an isotropic medium to methane diffusion, that is, $D_{\mathrm{C}} = D_{\mathrm{C},x} = D_{\mathrm{C},y} = D_{\mathrm{C},z}$. Error bars were computed via the sample variance of the results of at least five independent simulations.

Different symbols represent data where increasing equilibrium concentration, $c_{\mathrm{eq,zeol}}$, was achieved by changing the number of methane molecules while using a simulation box of (approximately) constant size. By contrast, the grey-shaded areas correspond to the opposite case where the simulation box size varies while the number of methane molecules is (roughly) the same. In doing so, we observe that the corrected diffusivity in LTA (on the right hand-side of Figure S7) exhibits a slight adsorbate-particle number influence which, however, levels off as soon as more than 100 methane molecules are simulated. This effect can be ascribed to the thermostat and it has been also reported by Dubbeldam et al.[32] The authors recommended to couple more than 100 particles to the thermostat to avoid this biasing effect.[32] We regard the thermostat influence to also be the reason why both the transport diffusivity and the surface permeability from TrMD in LTA increase slightly with sheet thickness ($D_{\mathrm{T}}^{\mathrm{loc}}$ and α^{loc} in Table 1 in main text). The thicker the sheet is, the higher will be the average number of molecules in the TrMD simulation at comparable uptake rates. The higher the average number of molecules, the larger the diffusion coefficient as a result of the thermostat effect. Since the surface permeability follows the same concentration behavior as the diffusivity (Figure S11), the same reasoning applies to α with respect to the thermostat

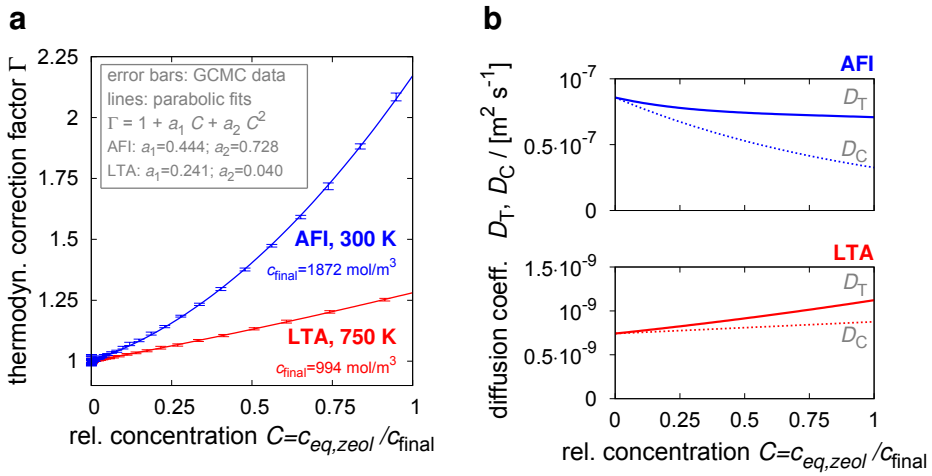

Figure S8: a) Thermodynamic correction factors, Γ, as functions of relative concentration, $C = c_{\mathrm{eq,zeol}}/c_{\mathrm{final}}$, for methane in AFI at 300 K and in LTA at 750 K. Since the data is somewhat noisy at low concentrations we have fitted the correction factor from GCMC (error bars) to parabolic functions (lines), providing excellent agreement. b) Transport, D_{T}, and corrected diffusion coefficients, D_{C}, vs relative concentration (same systems) where D_{C} is obtained from equilibrium MD simulations and converted to D_{T} with Γ via Eq. (12).

influence.

We have used analytic functions to describe the concentration dependence of D_{C} (dashed lines in Figure S7) for the determination of the transport-diffusion coefficient on the basis of EMD simulations. In the case of AFI, an exponential reproduced the trend best whereas a simple linear relationship was sufficient for LTA. Also, the thermodynamic correction factors, derived from the adsorption isotherm by numerical differentiation (error bars in Figure S8a), were fitted to analytical solutions (lines in Figure S8a). Here, a parabola worked best where Γ increases monotonically in the concentration range relevant to our TrMD simulations. In Figure S8b, both diffusion coefficients from equilibrium MD simulations are plotted over relative concentration, $c_{\mathrm{eq,zeol}}/c_{\mathrm{final}}$: the corrected diffusion coefficient (dotted lines) and the transport diffusivity (solid lines) for AFI (top) and LTA (bottom). The mean transport-diffusion coefficients, $\bar{D}_{\mathrm{T}}$, are hence 7.55×10^{-8} m^2/s and 9.2×10^{-10} m^2/s for AFI and LTA, respectively.

3 LTA Tracer-Exchange Surface Permeability

The surface permeability, α_S, of methane under tracer-exchange conditions in LTA was determined by means of a prediction[5] that is grounded on dynamically corrected transition state theory[37–39] and the assumption that the interface between gas and solid consists of two sublayers[5,40] (cf., Figure 2 in ref 5):

$$\alpha_S = \frac{\bar{v}/c_{eq,zeol}}{1/(\kappa_{gas}c^*_{eq,gas}) + 1/(\kappa_{surf}c^*_{eq,surf})}. \quad (13)$$

In Eq. (13), $\bar{v}$ denotes the average directed velocity of a methane molecule along the z coordinate which equals $\sqrt{k_B T/(2\pi m)}$, $c_{eq,zeol}$ the average equilibrium concentration throughout the zeolite nanosheet whereas $c^*_{eq,gas}$ and $c^*_{eq,surf}$ denote the equilibrium concentrations at the positions of the transition states for methane molecules moving between the surface adsorption layer and the gas space as well as between the surface adsorption layer and the outermost zeolite cage, and κ_{gas} and κ_{surf} are the corresponding transmission coefficients for crossing the just mentioned transition states. Note that we have used here subscript "eq" to signify that the concentrations refer to equilibrium profiles along the simulation box obtained from standard NVT Monte Carlo simulations.

Before we show the results, we have to highlight two differences in comparison to our recent approach to predict α_S via Eq. (13). First, the surfaces of the LTA nanosheets have regularly distributed hollows (Figure 1 in the main text) which complicate the calculation of concentration profiles and thus evaluation of Eq. (13). The problem becomes more tangible by considering Figure S9, where we provide two-dimensional free-energy landscapes of methane in the interface region between gas phase and zeolite interior. Marked with large "O" and large "X", we highlight the transition state location for methane molecules traveling from the outermost cage to the surface adsorption layer and the location of the adsorption site in this layer. Clearly, if we used simple concentration profiles along z the low concentration at the transition state "O" (i.e., $c^*_{eq,surf}$) would be superimposed by the high concentration of the surface adsorption layer at "X", therefore leading to an artificial increase of the surface permeability. To avoid this, we turned back to the three-dimensional residence distributions on which Figure S9 is actually based and directly evaluated

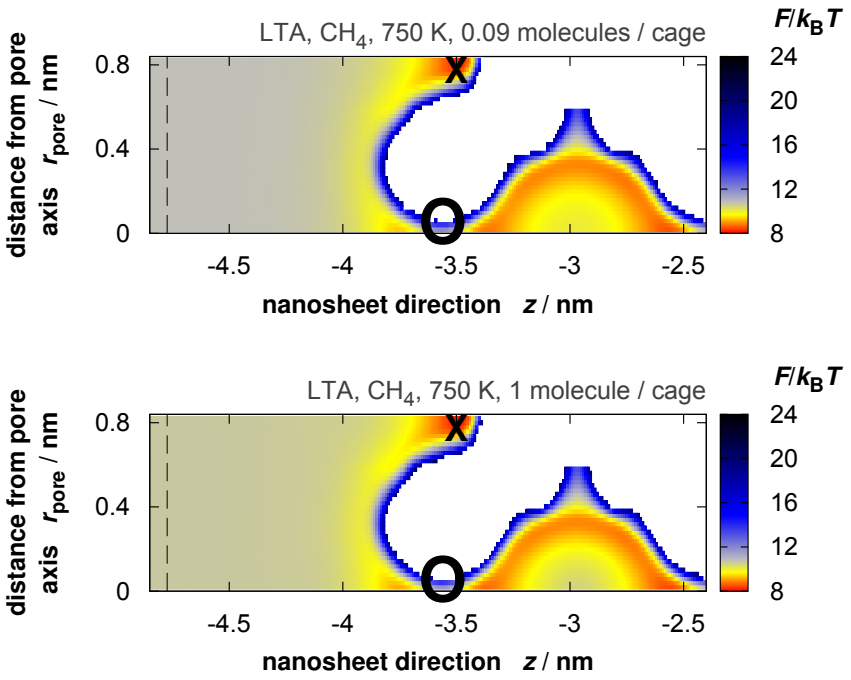

Figure S9: Two-dimensional free-energy landscapes, $F(z,r_{\mathrm{pore}})/k_{\mathrm{B}}T$, of methane in the interface between LTA nanosheet interior (right hand-side) and gas space (left hand-side) for two different average zeolite loadings. White areas indicate regions that were never visited by a methane molecule, black and blue regions are rarely visited regions, and red frequently visited regions. The landscapes are based on three-dimensional residence probability distributions of methane molecules in the simulation box, where it is important to underline that they were corrected for a non-linear mapping of the Cartesian x and y coordinate. That is, $F(z,r_{\mathrm{pore}})/k_{\mathrm{B}}T = -\ln[N_{\mathrm{hits}}(z,r_{\mathrm{pore}})/r_{\mathrm{pore}}^2]$, where $N_{\mathrm{hits}}(z,r_{\mathrm{pore}})$ denotes the accumulated, *not the averaged* number of hits of having found a molecule at z and a distance r_{pore} apart from the pore axis with respect to x and y.

the number of hits in each voxel, $N_{\mathrm{hits}}(x,y,z)$. Therefore, $c_{\mathrm{eq,zeol}}$ was substituted by the number of hits averaged over all voxels that belonged to the innermost cage, $\bar{N}_{\mathrm{hits,zeol}}$. Likewise, $c^*_{\mathrm{eq,surf}}$ was obtained by averaging the number of hits, $\bar{N}^*_{\mathrm{hits,surf}}$, in the plane at $z = -3.57$ nm (position of outermost zeolite atoms) with the restriction that voxels were included for averaging only if they were at most 0.15 nm apart from the pore axis along z. Finally, $c^*_{\mathrm{eq,gas}}$ was substituted by the number of hits, $\bar{N}^*_{\mathrm{hits,gas}}$, averaged over the separation plane between surface adsorption layer and gas phase (dashed lines in Figure S9). To test its validity, we have calculated the concentration-dependent self-diffusion coefficients based on transition state theory employing the 3D distribution

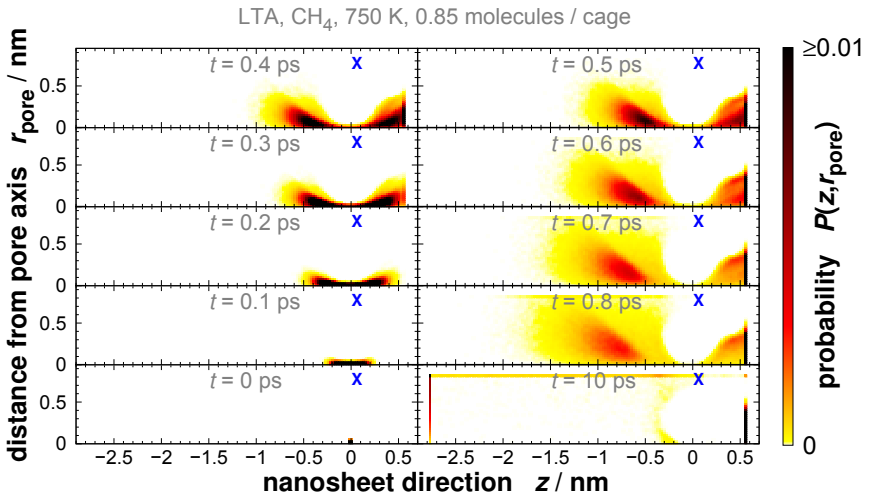

Figure S10: Evolution of a swarm of reactive flux trajectories leaving the surface barrier between external adsorption layer and outermost zeolite cage. Note that we have shifted the origin of the z coordinate to the location of the surface barrier in comparison to Figure S9 where it is found at $z = -3.57$ nm.

analysis which gave identical results in comparison to conventional 1D histogram analysis.

The second difference was also due to the structure of the LTA surface and concerned the transmission coefficients. The location of the surface adsorption site would have also required an additional order parameter, such as the distance from the pore axis, r_{pore}, to be used in the reactive flux (RF) simulations for determination of the transmission coefficients. This is, because the final state for a methane molecule hopping either from the outermost cage onto the surface layer (κ_{surf}) or for a movement from the gas phase towards the surface layer (κ_{gas}) is not unequivocal with a simple one-dimensional reaction coordinate. Despite this problem, we find that it is sufficient to start the RF simulations from the surface barrier ("O" in Figure S9) and stop a given shoot if the molecule has reached either the center plane of the outermost cage ($z = 2.95$ nm) or if it has left the simulation box at the left hand-side end at $z = 6.34$ nm. Evidence comes from probability distributions that track the temporal evolution of the entire swarm of RF trajectories,[41,42] as displayed in Figure S10. Only a very small fraction of the swarm aims for the surface adsorption site, which is again marked with an "X" (blue). This fact leads finally to the vast majority of RF trajectories arriving either at the left boundary of the surface adsorption layer ($z = -2.8$ nm in

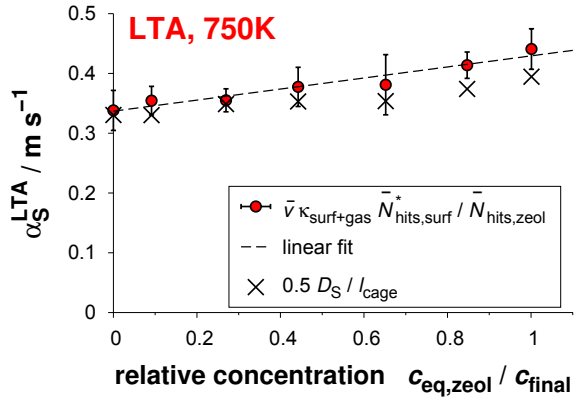

Figure S11: Tracer-exchange surface permeability prediction, α_S^{LTA}, of methane through the LTA nanosheet interface over relative zeolite concentration, $c_{eq,zeol}/c_{final}$, at 750 K.

Figure S10) or at the right boundary of the outermost cage ($z = 0.55$ nm in Figure S10) after 10 ps. Hence, a negligibly small number of trajectories is "caught" between the surface adsorption layer and gas phase only. We conclude therefore that neither $\bar{N}^*_{hits,gas}$ nor κ_{gas} is actually needed because methane molecules on the surface barrier commit directly to either the gas phase or the zeolite interior. Hence, we can in good approximation predict α_S by:

$$\alpha_S^{LTA} = \frac{\bar{v}\kappa_{surf+gas}\bar{N}^*_{hits,surf}}{N_{hits,zeol}}. \tag{14}$$

Here $\kappa_{surf+gas}$ is the combined transmission coefficient for methane molecules starting from the surface barrier and ending up in either the outermost zeolite cage or in the gas phase.

Finally, we have plotted the resulting tracer-exchange surface permeability prediction of methane through the interface of the LTA nanosheet over the relative concentration, $c_{eq,zeol}/c_{final}$, in Figure S11 (circles). In addition, we provide a linear fit to the data points by which means we have determined the mean surface permeability to 0.383 m/s and we show also a surface permeability prediction on the basis of the self-diffusion coefficient[43] (crosses). It is furthermore instructive to mention that the corrected diffusivity is identical to the self-diffusion coefficient in the concentration range of Figure S11.

4 Concentration-Dependent Corrected Diffusivity from TrMD

As mentioned in Table 1 in the text, we have also fitted the analytical solutions of the concentration profiles with the surface-barrier boundary condition to our transient MD data by introducing a third parameter. That parameter describes the concentration dependence of the corrected diffusion coefficient. In agreement with our EMD findings (Section 2.2), we employ an exponential function in case of AFI

$$D_{\mathrm{C}}(c) = D_{\mathrm{C},0} \cdot \exp(a_3 \cdot c) \tag{15}$$

and a linear relationship for LTA

$$D_{\mathrm{C}}(c) = D_{\mathrm{C},0} + a_4 \cdot c, \tag{16}$$

with $D_{\mathrm{C},0}$ the zero-concentration diffusivity and a_3 as well as a_4 being constant. Obviously, we have also to input the thermodynamic correction factor into our fitting approach. This was actually the reason why we have introduced analytical descriptions of Γ in Section 2.2 in the first place because they are easier to handle during fitting than any discrete data sets on Γ. Finally, note that we used the average methane concentration throughout the entire nanosheet, $\overline{c}(t_i)$, at a given instance of time for the determination of the "instantaneous" concentration-dependent transport-diffusion coefficient, $D_{\mathrm{T}}(t) = D_{\mathrm{C}}[\overline{c}(t_i)] \times \Gamma[\overline{c}(t_i)]$, and thus for calculation of the concentration profile at time instance t_i.

The results are presented in Table S1 along with the mean transport diffusivity resulting from the fitted functionals. The mean diffusivities and also the surface permeabilities agree very well with those presented in the main text for fitting of c-profiles with α and a *constant* D_{T}. However, the fitted parameters are consistent with the one from EMD simulations in the case of AFI only. As Figure S12 shows, EMD data and TrMD fits fall on top of one another for AFI whereas we observe strong deviations for LTA. The fact that the mean transport-diffusivity is nonetheless consistent with the average derived in Section 2.2 leads to the conclusion that the concentration dependence of the diffusivity does not play as important a role for methane uptake into very thin LTA nanosheets as into AFI sheets.

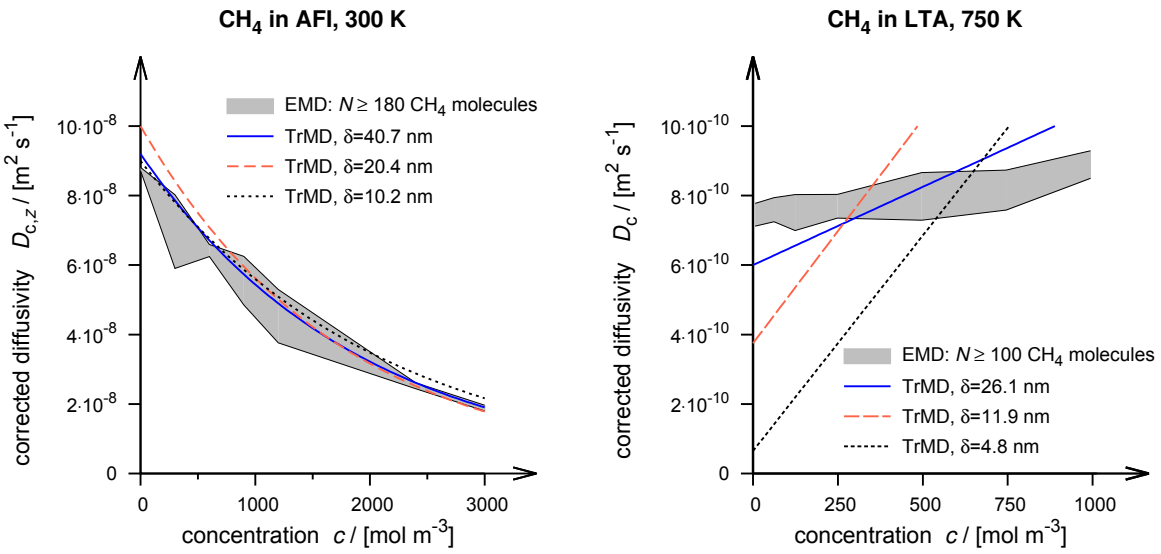

Figure S12: Corrected diffusion coefficients of methane in AFI at 300 K (left) and LTA at 750 K (right) from equilibrium molecular dynamics simulations (*NVT*) and from fitting analytical solutions of concentration profiles to data from transient molecular dynamics simulations where a concentration-dependent diffusion coefficient was used in the analytical solutions.

Table S1: Surface Permeabilities and Concentration-Dependent Diffusion Coefficients.

	δ [nm]	α [m/s]	$D_{C,0}$ [10^{-10}m^2/s]	a_3, a_4 [10^{-3}m^3/mol] [10^{-13}m^5/(s mol)]	σ_{rel}[a] [%]	$\bar{D}_T^{loc}$ [b] [10^{-10}m^2/s]
AFI	10.2	10.6	900	−0.475	3.6	823
	20.4	8.9	1000	−0.575	3.3	835
	40.7	7.9	920	−0.525	3.4	804
LTA	4.8	0.27	0.65	12.4	3.7	8.01
	11.9	0.29	3.75	12.9	3.3	11.82
	26.1	0.34	6.00	4.5	3.1	9.44

[a] *Relative sample standard deviation averaged over all data points.* [b] *Average transport-diffusion coefficient obtained from these fits and thus not from EMD as in main text.*

5 Crystal Structures

5.1 LTA

```
                                    11.8671   11.8671   11.8671
                     90.000  90.000  90.000    SPGR =  1 P 1         OPT = 1
  72   0
     0 LTA         : LTA
1 O1   0.0   0.21790000000000001   0.5   0 0 0 0 0 0 0 0 0.00
2 O1   0.0   0.5   0.21790000000000001   0 0 0 0 0 0 0 0 0.00
3 O1   0.0   0.5   0.78210000000000002   0 0 0 0 0 0 0 0 0.00
4 O1   0.5   0.21790000000000001   0.0   0 0 0 0 0 0 0 0 0.00
5 O1   0.78210000000000002   0.0   0.5   0 0 0 0 0 0 0 0 0.00
6 O1   0.21790000000000001   0.0   0.5   0 0 0 0 0 0 0 0 0.00
7 O1   0.5   0.0   0.21790000000000001   0 0 0 0 0 0 0 0 0.00
8 O1   0.21790000000000001   0.5   0.0   0 0 0 0 0 0 0 0 0.00
9 O1   0.78210000000000002   0.5   0.0   0 0 0 0 0 0 0 0 0.00
10 O1   0.5   0.0   0.78210000000000002   0 0 0 0 0 0 0 0 0.00
11 O1   0.0   0.78210000000000002   0.5   0 0 0 0 0 0 0 0 0.00
12 O1   0.5   0.78210000000000002   0.0   0 0 0 0 0 0 0 0 0.00
13 O2   0.10979999999999999   0.10979999999999999   0.34289999999999998   0 0 0 0 0 0 0 0 0.00
14 O2   0.10979999999999999   0.65710000000000002   0.10979999999999999   0 0 0 0 0 0 0 0 0.00
15 O2   0.10979999999999999   0.34289999999999998   0.89019999999999999   0 0 0 0 0 0 0 0 0.00
16 O2   0.34289999999999998   0.10979999999999999   0.89019999999999999   0 0 0 0 0 0 0 0 0.00
17 O2   0.65710000000000002   0.10979999999999999   0.10979999999999999   0 0 0 0 0 0 0 0 0.00
18 O2   0.89019999999999999   0.10979999999999999   0.34289999999999998   0 0 0 0 0 0 0 0 0.00
19 O2   0.10979999999999999   0.89019999999999999   0.34289999999999998   0 0 0 0 0 0 0 0 0.00
20 O2   0.34289999999999998   0.10979999999999999   0.10979999999999999   0 0 0 0 0 0 0 0 0.00
21 O2   0.10979999999999999   0.34289999999999998   0.10979999999999999   0 0 0 0 0 0 0 0 0.00
22 O2   0.89019999999999999   0.65710000000000002   0.10979999999999999   0 0 0 0 0 0 0 0 0.00
23 O2   0.34289999999999998   0.89019999999999999   0.89019999999999999   0 0 0 0 0 0 0 0 0.00
24 O2   0.89019999999999999   0.34289999999999998   0.89019999999999999   0 0 0 0 0 0 0 0 0.00
25 O2   0.65710000000000002   0.89019999999999999   0.10979999999999999   0 0 0 0 0 0 0 0 0.00
26 O2   0.65710000000000002   0.10979999999999999   0.89019999999999999   0 0 0 0 0 0 0 0 0.00
27 O2   0.10979999999999999   0.65710000000000002   0.89019999999999999   0 0 0 0 0 0 0 0 0.00
28 O2   0.10979999999999999   0.89019999999999999   0.65710000000000002   0 0 0 0 0 0 0 0 0.00
29 O2   0.89019999999999999   0.10979999999999999   0.65710000000000002   0 0 0 0 0 0 0 0 0.00
30 O2   0.89019999999999999   0.89019999999999999   0.34289999999999998   0 0 0 0 0 0 0 0 0.00
31 O2   0.10979999999999999   0.10979999999999999   0.65710000000000002   0 0 0 0 0 0 0 0 0.00
32 O2   0.89019999999999999   0.89019999999999999   0.65710000000000002   0 0 0 0 0 0 0 0 0.00
33 O2   0.34289999999999998   0.89019999999999999   0.10979999999999999   0 0 0 0 0 0 0 0 0.00
```

```
34 O2   0.65710000000000002   0.89019999999999999   0.89019999999999999   0 0 0 0 0 0 0 0 0.00
35 O2   0.89019999999999999   0.34289999999999998   0.10979999999999999   0 0 0 0 0 0 0 0 0.00
36 O2   0.89019999999999999   0.65710000000000002   0.89019999999999999   0 0 0 0 0 0 0 0 0.00
37 O3   0.0   0.29389999999999999   0.29389999999999999   0 0 0 0 0 0 0 0 0.00
38 O3   0.0   0.70609999999999995   0.29389999999999999   0 0 0 0 0 0 0 0 0.00
39 O3   0.0   0.29389999999999999   0.70609999999999995   0 0 0 0 0 0 0 0 0.00
40 O3   0.29389999999999999   0.29389999999999999   0.0   0 0 0 0 0 0 0 0 0.00
41 O3   0.70609999999999995   0.29389999999999999   0.0   0 0 0 0 0 0 0 0 0.00
42 O3   0.70609999999999995   0.0   0.29389999999999999   0 0 0 0 0 0 0 0 0.00
43 O3   0.29389999999999999   0.0   0.29389999999999999   0 0 0 0 0 0 0 0 0.00
44 O3   0.70609999999999995   0.70609999999999995   0.0   0 0 0 0 0 0 0 0 0.00
45 O3   0.29389999999999999   0.0   0.70609999999999995   0 0 0 0 0 0 0 0 0.00
46 O3   0.70609999999999995   0.0   0.70609999999999995   0 0 0 0 0 0 0 0 0.00
47 O3   0.29389999999999999   0.70609999999999995   0.0   0 0 0 0 0 0 0 0 0.00
48 O3   0.0   0.70609999999999995   0.70609999999999995   0 0 0 0 0 0 0 0 0.00
49 Si1   0.0   0.1847   0.36830000000000002   0 0 0 0 0 0 0 0 0.00
50 Si1   0.0   0.63169999999999993   0.1847   0 0 0 0 0 0 0 0 0.00
51 Si1   0.0   0.36830000000000002   0.81530000000000002   0 0 0 0 0 0 0 0 0.00
52 Si1   0.36830000000000002   0.1847   0.0   0 0 0 0 0 0 0 0 0.00
53 Si1   0.63169999999999993   0.1847   0.0   0 0 0 0 0 0 0 0 0.00
54 Si1   0.81530000000000002   0.0   0.36830000000000002   0 0 0 0 0 0 0 0 0.00
55 Si1   0.1847   0.0   0.36830000000000002   0 0 0 0 0 0 0 0 0.00
56 Si1   0.36830000000000002   0.0   0.1847   0 0 0 0 0 0 0 0 0.00
57 Si1   0.1847   0.36830000000000002   0.0   0 0 0 0 0 0 0 0 0.00
58 Si1   0.81530000000000002   0.63169999999999993   0.0   0 0 0 0 0 0 0 0 0.00
59 Si1   0.36830000000000002   0.0   0.81530000000000002   0 0 0 0 0 0 0 0 0.00
60 Si1   0.81530000000000002   0.36830000000000002   0.0   0 0 0 0 0 0 0 0 0.00
61 Si1   0.63169999999999993   0.0   0.1847   0 0 0 0 0 0 0 0 0.00
62 Si1   0.63169999999999993   0.0   0.81530000000000002   0 0 0 0 0 0 0 0 0.00
63 Si1   0.1847   0.63169999999999993   0.0   0 0 0 0 0 0 0 0 0.00
64 Si1   0.0   0.81530000000000002   0.63169999999999993   0 0 0 0 0 0 0 0 0.00
65 Si1   0.0   0.1847   0.63169999999999993   0 0 0 0 0 0 0 0 0.00
66 Si1   0.0   0.81530000000000002   0.36830000000000002   0 0 0 0 0 0 0 0 0.00
67 Si1   0.1847   0.0   0.63169999999999993   0 0 0 0 0 0 0 0 0.00
68 Si1   0.81530000000000002   0.0   0.63169999999999993   0 0 0 0 0 0 0 0 0.00
69 Si1   0.36830000000000002   0.81530000000000002   0.0   0 0 0 0 0 0 0 0 0.00
70 Si1   0.63169999999999993   0.81530000000000002   0.0   0 0 0 0 0 0 0 0 0.00
71 Si1   0.0   0.36830000000000002   0.1847   0 0 0 0 0 0 0 0 0.00
72 Si1   0.0   0.63169999999999993   0.81530000000000002   0 0 0 0 0 0 0 0 0.00
```

5.2 AFI

```
                                    23.774  13.726   8.484
                     90.000  90.000  90.000    SPGR =  1 P 1         OPT = 1
 144   0
     0 AFI         : AFI
   1 Si1      0.22620   0.10210   0.07800    5   7   9  11   0   0   0   0   0.000
   2 Si2      0.72620   0.60210   0.07800    6   8  10  12   0   0   0   0   0.000
   3 Si3     0.22885   0.10885   0.45000    7  83 101 117   0   0   0   0   0.000
   4 Si4     0.72885   0.60885   0.45000    8  84 102 118   0   0   0   0   0.000
   5 O5      0.21050   0.00320   0.02800    1   0   0   0   0   0   0   0   0.000
   6 O6      0.71050   0.50320   0.02800    2   0   0   0   0   0   0   0   0.000
   7 O7      0.22775   0.10345   0.25000    1   3   0   0   0   0   0   0   0.000
   8 O8      0.72775   0.60345   0.25000    2   4   0   0   0   0   0   0   0.000
   9 O9      0.18350   0.17490   0.02600    1   0   0   0   0   0   0   0   0.000
  10 O10     0.68350   0.67490   0.02600    2   0   0   0   0   0   0   0   0.000
  11 O11     0.28420   0.12840   0.01400    1   0   0   0   0   0   0   0   0.000
  12 O12     0.78420   0.62840   0.01400    2   0   0   0   0   0   0   0   0.000
  13 Si13     0.33585   0.78825   0.07800   17  19  21  23   0   0   0   0   0.000
  14 Si14     0.83585   0.28825   0.07800   18  20  22  24   0   0   0   0   0.000
  15 Si15    0.33115   0.78885   0.45000   19  89 107 141   0   0   0   0   0.000
  16 Si16    0.83115   0.28885   0.45000   20  90 108 142   0   0   0   0   0.000
  17 O17     0.39315   0.81415   0.02800   13   0   0   0   0   0   0   0   0.000
  18 O18     0.89315   0.31415   0.02800   14   0   0   0   0   0   0   0   0.000
  19 O19     0.33440   0.78990   0.25000   13  15   0   0   0   0   0   0   0.000
  20 O20     0.83440   0.28990   0.25000   14  16   0   0   0   0   0   0   0.000
  21 O21     0.32080   0.68780   0.02600   13   0   0   0   0   0   0   0   0.000
  22 O22     0.82080   0.18780   0.02600   14   0   0   0   0   0   0   0   0.000
  23 O23     0.29370   0.86210   0.01400   13   0   0   0   0   0   0   0   0.000
  24 O24     0.79370   0.36210   0.01400   14   0   0   0   0   0   0   0   0.000
  25 Si25     0.43795   0.10965   0.07800   29  31  33  35   0   0   0   0   0.000
  26 Si26     0.93795   0.60965   0.07800   30  32   0  36   0   0   0   0   0.000
  27 Si27    0.44000   0.10230   0.45000   31  77   0 130   0   0   0   0   0.000
  28 Si28    0.94000   0.60230   0.45000   32  78  96   0   0   0   0   0   0.000
  29 O29     0.39635   0.18265   0.02800   25   0   0   0   0   0   0   0   0.000
  30 O30     0.89635   0.68265   0.02800   26   0   0   0   0   0   0   0   0.000
  31 O31     0.43785   0.10665   0.25000   25  27   0   0   0   0   0   0   0.000
  32 O32     0.93785   0.60665   0.25000   26  28   0   0   0   0   0   0   0.000
  33 O33     0.49570   0.13730   0.02600   25   0   0   0   0   0   0   0   0.000
  34 O34    -0.00430   0.63730   0.02600    0   0   0   0   0   0   0   0   0.000
  35 O35     0.42210   0.00950   0.01400   25   0   0   0   0   0   0   0   0.000
  36 O36     0.92210   0.50950   0.01400   26   0   0   0   0   0   0   0   0.000
```

37	Si37	0.27380	0.39790	0.07800	41	43	45	47	0	0	0	0	0.000
38	Si38	0.77380	0.89790	0.07800	0	44	46	48	0	0	0	0	0.000
39	Si39	0.27115	0.39115	0.45000	43	81	119	137	0	0	0	0	0.000
40	Si40	0.77115	0.89115	0.45000	44	82	120	0	0	0	0	0	0.000
41	O41	0.28950	0.49680	0.02800	37	0	0	0	0	0	0	0	0.000
42	O42	0.78950	-0.00320	0.02800	0	0	0	0	0	0	0	0	0.000
43	O43	0.27225	0.39655	0.25000	37	39	0	0	0	0	0	0	0.000
44	O44	0.77225	0.89655	0.25000	38	40	0	0	0	0	0	0	0.000
45	O45	0.31650	0.32510	0.02600	37	0	0	0	0	0	0	0	0.000
46	O46	0.81650	0.82510	0.02600	38	0	0	0	0	0	0	0	0.000
47	O47	0.21580	0.37160	0.01400	37	0	0	0	0	0	0	0	0.000
48	O48	0.71580	0.87160	0.01400	38	0	0	0	0	0	0	0	0.000
49	Si49	0.16415	0.71175	0.07800	53	55	57	59	0	0	0	0	0.000
50	Si50	0.66415	0.21175	0.07800	54	56	58	60	0	0	0	0	0.000
51	Si51	0.16885	0.71115	0.45000	55	105	125	143	0	0	0	0	0.000
52	Si52	0.66885	0.21115	0.45000	56	106	126	144	0	0	0	0	0.000
53	O53	0.10685	0.68585	0.02800	49	0	0	0	0	0	0	0	0.000
54	O54	0.60685	0.18585	0.02800	50	0	0	0	0	0	0	0	0.000
55	O55	0.16560	0.71010	0.25000	49	51	0	0	0	0	0	0	0.000
56	O56	0.66560	0.21010	0.25000	50	52	0	0	0	0	0	0	0.000
57	O57	0.17920	0.81220	0.02600	49	0	0	0	0	0	0	0	0.000
58	O58	0.67920	0.31220	0.02600	50	0	0	0	0	0	0	0	0.000
59	O59	0.20630	0.63790	0.01400	49	0	0	0	0	0	0	0	0.000
60	O60	0.70630	0.13790	0.01400	50	0	0	0	0	0	0	0	0.000
61	Si61	0.06205	0.39035	0.07800	65	67	69	71	0	0	0	0	0.000
62	Si62	0.56205	0.89035	0.07800	66	68	70	72	0	0	0	0	0.000
63	Si63	0.06000	0.39770	0.45000	67	94	113	131	0	0	0	0	0.000
64	Si64	0.56000	0.89770	0.45000	68	93	114	0	0	0	0	0	0.000
65	O65	0.10365	0.31735	0.02800	61	0	0	0	0	0	0	0	0.000
66	O66	0.60365	0.81735	0.02800	62	0	0	0	0	0	0	0	0.000
67	O67	0.06215	0.39335	0.25000	61	63	0	0	0	0	0	0	0.000
68	O68	0.56215	0.89335	0.25000	62	64	0	0	0	0	0	0	0.000
69	O69	0.00430	0.36270	0.02600	61	0	0	0	0	0	0	0	0.000
70	O70	0.50430	0.86270	0.02600	62	0	0	0	0	0	0	0	0.000
71	O71	0.07790	0.49050	0.01400	61	0	0	0	0	0	0	0	0.000
72	O72	0.57790	0.99050	0.01400	62	0	0	0	0	0	0	0	0.000
73	Si73	0.33585	0.21175	0.57800	77	79	81	83	0	0	0	0	0.000
74	Si74	0.83585	0.71175	0.57800	78	80	82	84	0	0	0	0	0.000
75	Si75	0.33115	0.21115	0.95000	0	0	0	79	0	0	0	0	0.000
76	Si76	0.83115	0.71115	0.95000	0	0	0	80	0	0	0	0	0.000
77	O77	0.39315	0.18585	0.52800	27	73	0	0	0	0	0	0	0.000

78	O78	0.89315	0.68585	0.52800	28	74	0	0	0	0	0	0	0.000
79	O79	0.33440	0.21010	0.75000	73	75	0	0	0	0	0	0	0.000
80	O80	0.83440	0.71010	0.75000	74	76	0	0	0	0	0	0	0.000
81	O81	0.32080	0.31220	0.52600	39	73	0	0	0	0	0	0	0.000
82	O82	0.82080	0.81220	0.52600	40	74	0	0	0	0	0	0	0.000
83	O83	0.29370	0.13790	0.51400	3	73	0	0	0	0	0	0	0.000
84	O84	0.79370	0.63790	0.51400	4	74	0	0	0	0	0	0	0.000
85	Si85	0.43795	0.89035	0.57800	89	91	93	95	0	0	0	0	0.000
86	Si86	0.93795	0.39035	0.57800	90	92	0	96	0	0	0	0	0.000
87	Si87	0.44000	0.89770	0.95000	0	0	0	91	0	0	0	0	0.000
88	Si88	0.94000	0.39770	0.95000	0	0	0	92	0	0	0	0	0.000
89	O89	0.39635	0.81735	0.52800	15	85	0	0	0	0	0	0	0.000
90	O90	0.89635	0.31735	0.52800	16	86	0	0	0	0	0	0	0.000
91	O91	0.43785	0.89335	0.75000	85	87	0	0	0	0	0	0	0.000
92	O92	0.93785	0.39335	0.75000	86	88	0	0	0	0	0	0	0.000
93	O93	0.49570	0.86270	0.52600	64	85	0	0	0	0	0	0	0.000
94	O94	-0.00430	0.36270	0.52600	63	0	0	0	0	0	0	0	0.000
95	O95	0.42210	0.99050	0.51400	0	85	0	0	0	0	0	0	0.000
96	O96	0.92210	0.49050	0.51400	28	86	0	0	0	0	0	0	0.000
97	Si97	0.22620	0.89790	0.57800	0	103	105	107	0	0	0	0	0.000
98	Si98	0.72620	0.39790	0.57800	102	104	106	108	0	0	0	0	0.000
99	Si99	0.22885	0.89115	0.95000	0	0	0	103	0	0	0	0	0.000
100	Si0	0.72885	0.39115	0.95000	0	0	0	104	0	0	0	0	0.000
101	O101	0.21050	-0.00320	0.52800	3	0	0	0	0	0	0	0	0.000
102	O102	0.71050	0.49680	0.52800	4	98	0	0	0	0	0	0	0.000
103	O103	0.22775	0.89655	0.75000	97	99	0	0	0	0	0	0	0.000
104	O104	0.72775	0.39655	0.75000	98	100	0	0	0	0	0	0	0.000
105	O105	0.18350	0.82510	0.52600	51	97	0	0	0	0	0	0	0.000
106	O106	0.68350	0.32510	0.52600	52	98	0	0	0	0	0	0	0.000
107	O107	0.28420	0.87160	0.51400	15	97	0	0	0	0	0	0	0.000
108	O108	0.78420	0.37160	0.51400	16	98	0	0	0	0	0	0	0.000
109	Si109	0.16415	0.28825	0.57800	113	115	117	119	0	0	0	0	0.000
110	Si110	0.66415	0.78825	0.57800	114	116	118	120	0	0	0	0	0.000
111	Si11	0.16885	0.28885	0.95000	0	0	0	115	0	0	0	0	0.000
112	Si12	0.66885	0.78885	0.95000	0	0	0	116	0	0	0	0	0.000
113	O113	0.10685	0.31415	0.52800	63	109	0	0	0	0	0	0	0.000
114	O114	0.60685	0.81415	0.52800	64	110	0	0	0	0	0	0	0.000
115	O115	0.16560	0.28990	0.75000	109	111	0	0	0	0	0	0	0.000
116	O116	0.66560	0.78990	0.75000	110	112	0	0	0	0	0	0	0.000
117	O117	0.17920	0.18780	0.52600	3	109	0	0	0	0	0	0	0.000
118	O118	0.67920	0.68780	0.52600	4	110	0	0	0	0	0	0	0.000

```
119 O119    0.20630   0.36210   0.51400   39 109   0   0   0   0   0   0   0.000
120 O120    0.70630   0.86210   0.51400   40 110   0   0   0   0   0   0   0.000
121 Si121    0.06205   0.60965   0.57800  125 127 129 131   0   0   0   0   0.000
122 Si122    0.56205   0.10965   0.57800  126 128 130 132   0   0   0   0   0.000
123 Si23    0.06000   0.60230   0.95000    0   0   0 127   0   0   0   0   0.000
124 Si24    0.56000   0.10230   0.95000    0   0   0 128   0   0   0   0   0.000
125 O125    0.10365   0.68265   0.52800   51 121   0   0   0   0   0   0   0.000
126 O126    0.60365   0.18265   0.52800   52 122   0   0   0   0   0   0   0.000
127 O127    0.06215   0.60665   0.75000  121 123   0   0   0   0   0   0   0.000
128 O128    0.56215   0.10665   0.75000  122 124   0   0   0   0   0   0   0.000
129 O129    0.00430   0.63730   0.52600    0 121   0   0   0   0   0   0   0.000
130 O130    0.50430   0.13730   0.52600   27 122   0   0   0   0   0   0   0.000
131 O131    0.07790   0.50950   0.51400   63 121   0   0   0   0   0   0   0.000
132 O132    0.57790   0.00950   0.51400    0 122   0   0   0   0   0   0   0.000
133 Si133    0.27380   0.60210   0.57800  137 139 141 143   0   0   0   0   0.000
134 Si134    0.77380   0.10210   0.57800  138 140 142 144   0   0   0   0   0.000
135 Si35    0.27115   0.60885   0.95000    0   0   0 139   0   0   0   0   0.000
136 Si36    0.77115   0.10885   0.95000    0   0   0 140   0   0   0   0   0.000
137 O137    0.28950   0.50320   0.52800   39 133   0   0   0   0   0   0   0.000
138 O138    0.78950   0.00320   0.52800    0 134   0   0   0   0   0   0   0.000
139 O139    0.27225   0.60345   0.75000  133 135   0   0   0   0   0   0   0.000
140 O140    0.77225   0.10345   0.75000  134 136   0   0   0   0   0   0   0.000
141 O141    0.31650   0.67490   0.52600   15 133   0   0   0   0   0   0   0.000
142 O142    0.81650   0.17490   0.52600   16 134   0   0   0   0   0   0   0.000
143 O143    0.21580   0.62840   0.51400   51 133   0   0   0   0   0   0   0.000
144 O144    0.71580   0.12840   0.51400   52 134   0   0   0   0   0   0   0.000
```

6 List of Symbols

Symbol	Description	Units
a_1	parameter of analytical description of Γ	–
a_2	parameter of analytical description of Γ	–
a_3	parameter of analytical description of D_C in AFI	$\mathrm{m^3\ mol^{-1}}$
a_4	parameter of analytical description of D_C in LTA	$\mathrm{m^5\ mol^{-1}\ s^{-1}}$
$\mathrm{acc}(\mathscr{O} \to \mathscr{N})$	acceptance probability of a transition from state $\mathscr{O}$ to state $\mathscr{N}$	–
c	concentration	$\mathrm{mol\ m^{-3}}$
$\overline{c}(t_i)$	concentration at time instance t_i and averaged over the entire nanosheet (i.e., along z)	$\mathrm{mol\ m^{-3}}$
$\overline{c}(t_i, z_k)$	concentration at time instance t_i and position z_k averaged over 40 independent TrMD simulations	$\mathrm{mol\ m^{-3}}$
C	relative concentration [specifically: related to final TrMD state ($= c/c_\mathrm{final}$)]	–
D	diffusion coefficient	$\mathrm{m^2\ s^{-1}}$
$\overline{D}$	mean diffusion coefficient (specifically: averaged over concentration regime of interest)	$\mathrm{m^2\ s^{-1}}$
D_C	corrected diffusion coefficient	$\mathrm{m^2\ s^{-1}}$
$D_{\mathrm{C},0}$	parameter of analytical description of D_C	$\mathrm{m^2\ s^{-1}}$
D_S	self-diffusion coefficient	$\mathrm{m^2\ s^{-1}}$
D_T	transport-diffusion coefficient	$\mathrm{m^2\ s^{-1}}$
F	free energy	J
f	fugacity	Pa
h	Planck constant ($6.626068 \cdot 10^{-34}$)	J s
i	index variable	–
j	molar flux	$\mathrm{mol\ m^{-2}\ s^{-1}}$

To be continued on next page.

Symbol	Description	Units
K_{H}	Henry coefficient	mol Pa^{-1} kg^{-1}
k	index variable	–
k_{B}	Boltzmann constant ($1.3806488 \cdot 10^{-23}$)	$\mathrm{J\ K}^{-1}$
L	dimensionless coefficient [$\equiv (\delta/2)\alpha/D_{\mathrm{T}}$]	–
l	length or width	m
m	mass	kg
n	order of magnitude	–
N	number of molecules	–
N_{A}	Avogadro constant ($6.02214 \cdot 10^{23}$)	mol^{-1}
$N_{\mathrm{hits}}(x,y,z)$	number of hits of having found a molecule	
	at the given point in space	–
$\bar{N}_{\mathrm{hits}}$	average number of hits of having found a molecule	
	in some region to be specified	–
N_t	number of time instances of sampling c-profiles	
	in a TrMD simulation	–
N_{trials}	number of Monte Carlo trials	–
	(specifically: insertion plus deletion trials)	
$N_{\mathrm{uc},i}$	number of unit cells aligned along Cartesian coordinate i	–
N_z	number of points along z which a single c-profile	
	from a TrMD simulation consisted of	–
P	probability (density)	–
p	pressure	Pa
r	distance	m, Å
	[specifically: for atomic interaction calculation]	
r_{cutoff}	cutoff distance for interaction calculation	m, Å

To be continued on next page.

Symbol	Description	Units
r_{pore}	distance from pore axis	m
T	temperature	K
t	time	s
U	potential energy	J
V	volume	m^3
$\bar{v}$	mean velocity in one direction of one of the Cartesian coordinates (specifically: along z)	$\mathrm{m\ s}^{-1}$
x	Cartesian x-coordinate	m
y	Cartesian y-coordinate	m
z	Cartesian z-coordinate (specifically: coordinate along which uptake proceeds)	m
	Greek symbols	
α	surface permeability	$\mathrm{m\ s}^{-1}$
β	reciprocal temperature $[1/(k_{\mathrm{B}}T)]$	J^{-1}
γ_i	i-th positive root of $\gamma\tan\gamma = L$	–
Γ	thermodynamic correction factor $(\partial \ln f/\partial \ln c_{\mathrm{eq,zeol}}\vert_T)$	–
ε	Lennard-Jones well depth	J
δ	nanosheet thickness	m
κ	transmission coefficient	–
σ	Lennard-Jones zero-potential distance	m, Å
σ_{rel}	averaged relative sample standard deviation	%
θ	loading	molecules $\times(\mathrm{cage})^{-1}$
Λ	thermal de Broglie wavelength	m

To be continued on next page.

Symbol	Description	Units
μ	chemical potential	J mol^{-1}
π	3.141592653589793238	–

Superscript	Description
$*$	reference to a (free-energy) barrier
dcTST	reference to dynamically-corrected transition state theory
int	reference to an integral analytical diffusion solution
LTA	reference to LTA framework type
loc	reference to a spatially resolved (i.e., local) analytical diffusion solution

Subscript	Description
box	related to the simulation box
cage	related to a zeolite cage
cv	related to the control volume in transient molecular dynamics
eff	effective value (specifically: effective transport-diffusion coefficient, $D_{\mathrm{T,eff}}$)
eq	indicates an equilibrium (time-invariant) property
final	related to the final state in transient filling of a nanosheet
gas	related to the bulk gas phase
i	index (e.g. bead type, molecule number)
j	index
res	related to a (hypothetical, infinite) gas reservoir
slab	related to a slab of the nanosheet
surf	related to the surface separating the surface adsorption layer and the zeolite margin
S	related to self-diffusion and thus tracer-exchange situations
x	related to Cartesian x-coordinate
y	related to Cartesian y-coordinate
z	related to Cartesian z-coordinate
zeol	related to the bulk zeolite space

7 List of Abbreviations

Abbreviation	Meaning
CV	control volume
EMD	equilibrium molecular dynamics
GCMC	Grand-Canonical Monte Carlo
IFM	interference microscopy
NEMD	non-equilibrium molecular dynamics
MC	Monte Carlo
MD	molecular dynamics
MSD	mean squared displacement
RF	reactive flux
SMD	squared mean displacement
TrMD	transient molecular dynamics

References

(1) Hibbe, F.; Chmelik, C.; Heinke, L.; Pramanik, S.; Li, J.; Ruthven, D. M.; Tzoulaki, D.; Kärger, J. *J. Am. Chem. Soc.* **2011**, *133*, 2804–2807.

(2) Frenkel, D.; Smit, B. *Understanding Molecular Simulations: From Algorithms to Applications*; Academic Press: San Diego, USA, 2002.

(3) Thompho, S.; Chanajaree, R.; Remsungnen, T.; Hannongbua, S.; Bopp, P. A.; Fritzsche, S. *J. Phys. Chem. A* **2009**, *113*, 2004–2014.

(4) Martyna, G. J.; Tuckerman, M. E.; Tobias, D. J.; Klein, M. L. *Mol. Phys.* **1996**, *87*, 1117–1157.

(5) Zimmermann, N. E. R.; Smit, B.; Keil, F. J. *J. Phys. Chem. C* **2012**, *116*, 18878–18883.

(6) Dubbeldam, D.; Calero, S.; Vlugt, T. J. H.; Krishna, R.; Maesen, T. L. M.; Beerdsen, E.; Smit, B. *Phys. Rev. Lett.* **2004**, *93*, 088302.

(7) Newsome, D. A.; Sholl, D. S. *J. Phys. Chem. B* **2005**, *109*, 7237–7244.

(8) Dubbeldam, D.; Calero, S.; Vlugt, T. J. H.; Krishna, R.; Maesen, T. L. M.; Smit, B. *J. Phys. Chem. B* **2004**, *108*, 12301–12313.

(9) Vlugt, T. J. H.; Schenk, M. *J. Phys. Chem. B* **2002**, *106*, 12757–12763.

(10) Deem, M. W.; Newsam, J. M.; Creighton, J. A. *J. Am. Chem. Soc.* **1992**, *114*, 7198–7207.

(11) Smirnov, K. S.; Bougeard, D. *Zeolites* **1994**, *14*, 203–207.

(12) Zimmermann, N. E. R.; Jakobtorweihen, S.; Beerdsen, E.; Smit, B.; Keil, F. J. *J. Phys. Chem. C* **2007**, *111*, 17370–17381.

(13) García-Sánchez, A.; Dubbeldam, D.; Calero, S. *J. Phys. Chem. C* **2010**, *114*, 15068–15074.

(14) Krishna, R.; van Baten, J. M. *J. Phys. Chem. C* **2010**, *114*, 18017–18021.

(15) Krishna, R.; van Baten, J. M. *Microporous Mesoporous Mater.* **2011**, *137*, 83–91.

(16) Arya, G.; Chang, H.-C.; Maginn, E. J. *J. Chem. Phys.* **2001**, *115*, 8112–8124.

(17) R. F. Cracknell and D. Nicholson and N. Quirke, *Phys. Rev. Lett.* **1995**, *74*, 2463–2466.

(18) Beerdsen, E.; Dubbeldam, D.; Smit, B. *J. Phys. Chem. B* **2006**, *110*, 22754–22772.

(19) Corma, A.; Rey, F.; Rius, J.; Sabater, M. J.; Valencia, S. *Nature* **2004**, *431*, 287–290.

(20) Hedin, N.; DeMartin, G. J.; Roth, W. J.; Strohmaier, K. G.; Reyes, S. C. *Microporous Mesoporous Mater.* **2008**, *109*, 327–334.

(21) Palomino, M.; Corma, A.; Rey, F.; Valencia, S. *Langmuir* **2010**, *26*, 1910–1917.

(22) Zimmermann, N. E. R.; Haranczyk, M.; Sharma, M.; Liu, B.; Smit, B.; Keil, F. J. *Mol. Simul.* **2011**, *37*, 986–989.

(23) Hansen, N.; Krishna, R.; van Baten, J. M.; Bell, A. T.; Keil, F. J. *J. Phys. Chem. C* **2009**, *113*, 235–246.

(24) Kärger, J. *Microporous Mesoporous Mater.* **2008**, *116*, 715–717.

(25) Bialek, R.; Meier, W. M.; Davis, M.; Annen, M. J. *Zeolites* **1991**, *11*, 438–442.

(26) S. Qiu and W. Pang and H. Kessler and J. L. Guth, *Zeolites* **1989**, *9*, 440–444.

(27) Martin, C.; Coulomb, J. P.; Grillet, Y.; Kahn, R. *Fundamentals of Adsorption*; Kluwer Academic Publishers: Boston, USA, 1996; p 587.

(28) Martin, C.; Tosi-Pellenq, N.; Patarin, J.; Coulomb, J. P. *Langmuir* **1998**, *14*, 1774–1778.

(29) Song, L.; Sun, Z.; Duan, L.; Jiang, S.; Rees, L. V. C. *Studies in Surface Science and Catalysis* **2004**, *154*, 1797–1803.

(30) Nivarthi, S. S.; McCormick, A. V.; Davis, H. T. *Chem. Phys. Lett.* **1994**, *229*, 297–301.

(31) Jobic, H.; Hahn, K.; Kärger, J.; Bee, M.; Tuel, A.; Noack, M.; Girnus, I.; Kearley, G. J. *J. Phys. Chem. B* **1997**, *101*, 5834–5841.

(32) Dubbeldam, D.; Beerdsen, E.; Vlugt, T. J. H.; Smit, B. *J. Chem. Phys.* **2005**, *112*, 224712.

(33) Tzoulaki, D.; Heinke, L.; Castro, M.; Cubillas, P.; Anderson, M. W.; Zhou, W.; Wright, P. A.; Kärger, J. *J. Am. Chem. Soc.* **2010**, *132*, 11665–11670.

(34) Hampson, B.; Leach, H. F.; Lowe, B. M.; Williams, C. D. *Zeolites* **1989**, *9*, 521–525.

(35) Krishna, R.; van Baten, J. M. *Micropor. Mesopor. Mater.* **2008**, *109*, 91–108.

(36) Kärger, J.; Ruthven, D. M. *Diffusion in Zeolites and Other Microporous Solids*; John Wiley & Sons Inc.: New York, 1992.

(37) Bennett, C. H. *Thin Solid Films* **1975**, *25*, 65–70.

(38) Chandler, D. *J. Chem. Phys.* **1978**, *68*, 2959–2970.

(39) June, R. L.; Bell, A. T.; Theodorou, D. N. *J. Phys. Chem.* **1991**, *95*, 8866–8878.

(40) Schüring, A.; Gulín-González, J.; Vasenkov, S.; Fritzsche, S. *Micropor. Mesopor. Mater.* **2009**, *125*, 107–111.

(41) Peters, B.; Zimmermann, N. E. R.; Beckham, G. T.; Tester, J. W.; Trout, B. L. *J. Am. Chem. Soc.* **2008**, *130*, 17342–17350.

(42) Zimmermann, N. E. R.; Smit, B.; Keil, F. J. *J. Phys. Chem. C* **2010**, *114*, 300–310.

(43) Heinke, L.; Kärger, J. *Phys. Rev. Lett.* **2011**, *106*, 074501.